NANO LETTERS

Letter

pubs.acs.org/NanoLett

Tunable Positive to Negative Magnetoresistance in Atomically Thin WTe_2

Enze Zhang,[†,‡] Rui Chen,[†,‡] Ce Huang,[†,‡] Jihai Yu,[‡,§] Kaitai Zhang,[†] Weiyi Wang,[†,‡] Shanshan Liu,[†,‡] Jiwei Ling,[†,‡] Xiangang Wan,[‡,§] Hai-Zhou Lu,[∥] and Faxian Xiu*[,†,‡]

[†]State Key Laboratory of Surface Physics and Department of Physics, Fudan University, Shanghai 200433, China

[‡]Collaborative Innovation Center of Advanced Microstructures, Nanjing University, Nanjing 210093, China

[§]National Laboratory of Solid State Microstructures, School of Physics, Nanjing University, Nanjing 210093, China

[∥]Department of Physics, South University of Science and Technology of China, Shenzhen 518055, China

Supporting Information

ABSTRACT: Transitional metal ditelluride WTe_2 has been extensively studied owing to its intriguing physical properties like nonsaturating positive magnetoresistance and being possibly a type-II Weyl semimetal. While surging research activities were devoted to the understanding of its bulk properties, it remains a substantial challenge to explore the pristine physics in atomically thin WTe_2. Here, we report a successful synthesis of mono- to few-layer WTe_2 via chemical vapor deposition. Using atomically thin WTe_2 nanosheets, we discover a previously inaccessible ambipolar behavior that enables the tunability of magnetoconductance of few-layer WTe_2 from weak antilocalization to weak localization, revealing a strong electrical field modulation of the spin−orbit interaction under perpendicular magnetic field. These appealing physical properties unveiled in this study clearly identify WTe_2 as a promising platform for exotic electronic and spintronic device applications.

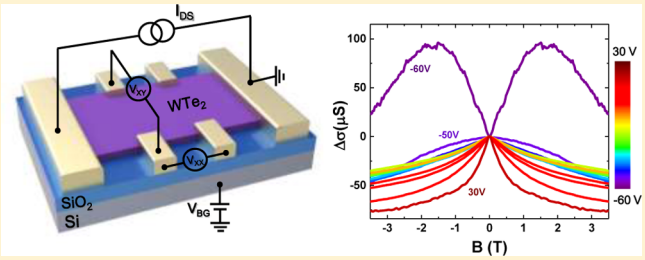

KEYWORDS: *WTe_2, negative magnetoresistance, ambipolar, weak antilocalization, weak localization, spin−orbit interaction*

The rise of graphene[1] has stimulated tremendous research interest in atomically thin two-dimensional (2D) materials like hexagonal boron nitride and transition metal chalcogenides (TMDs) with formula MX_2 (M = Mo, W; X = S, Se, Te).[2] Recently, WTe_2 has come to the front stage since the discovery of its extremely large positive magnetoresistance (MR) due to the perfect compensation of electron and hole bands.[3] Transport[4−7] and angle-resolved photoemission[8,9] experiments suggest a more complicated electronic structure of WTe_2 with more than two bands presenting at the Fermi level. More recently, theoretical calculations have predicted WTe_2 and $MoTe_2/Mo_xW_{1-x}Te_2$[10,11] to be possible candidates for the type-II Weyl semimetal, which fuel the continuous efforts in the investigation of the fine band structures in these materials.[12−21]

Interestingly, the monolayer WTe_2 was believed to be a quantum spin Hall insulator,[22,23] which makes WTe_2 a wonderful platform for investigating exotic physical phenomena and potential applications in spintronic and electronic devices. Mechanically exfoliated few-layer WTe_2 was demonstrated to have periodic Raman intensity variations due to the in-plane anisotropy of its crystal structure.[24,25] Also, as the thickness is reduced, WTe_2 exhibits strikingly different MR behavior from its bulk counterpart.[26,27] However, although WTe_2 can be exfoliated into few layers, the lack of gate tunability in its conductance and MR due to the high carrier density significantly hinders its further device applications. Chemical vapor deposition (CVD) has been proved to be an excellent approach to produce high-quality large-area monolayer and few-layer 2D materials like graphene[28] and MoS_2[29] that can be successfully integrated into electronic devices. Thus, it is of practical interest to grow large-scale atomically thin WTe_2 using the CVD method, and the gate-dependent magnetotransport properties of few-layer WTe_2 can be also anticipated.

Here, we report the CVD growth of atomically thin high-quality WTe_2, based on which the negative MR is observed when the magnetic field is parallel to the electrical field, indicative of a chiral anomaly. Four-terminal field-effect transistor (FET) devices clearly exhibit an ambipolar gate-dependent conductance at low temperatures. More importantly, owing to the effective modulation of the spin−orbit interaction by the applied perpendicular electric field, a systematic crossover from weak antilocalization (WAL) to weak localization (WL) is witnessed in few-layer WTe_2.

Monolayer and few-layer WTe_2 were synthesized onto SiO_2/Si substrates in a CVD tube furnace using tellurium powder and tungsten as the source materials (see Methods for details). As

Received: October 6, 2016
Revised: December 27, 2016
Published: December 29, 2016

ACS Publications © 2016 American Chemical Society

DOI: 10.1021/acs.nanolett.6b04194
Nano Lett. 2017, 17, 878−885

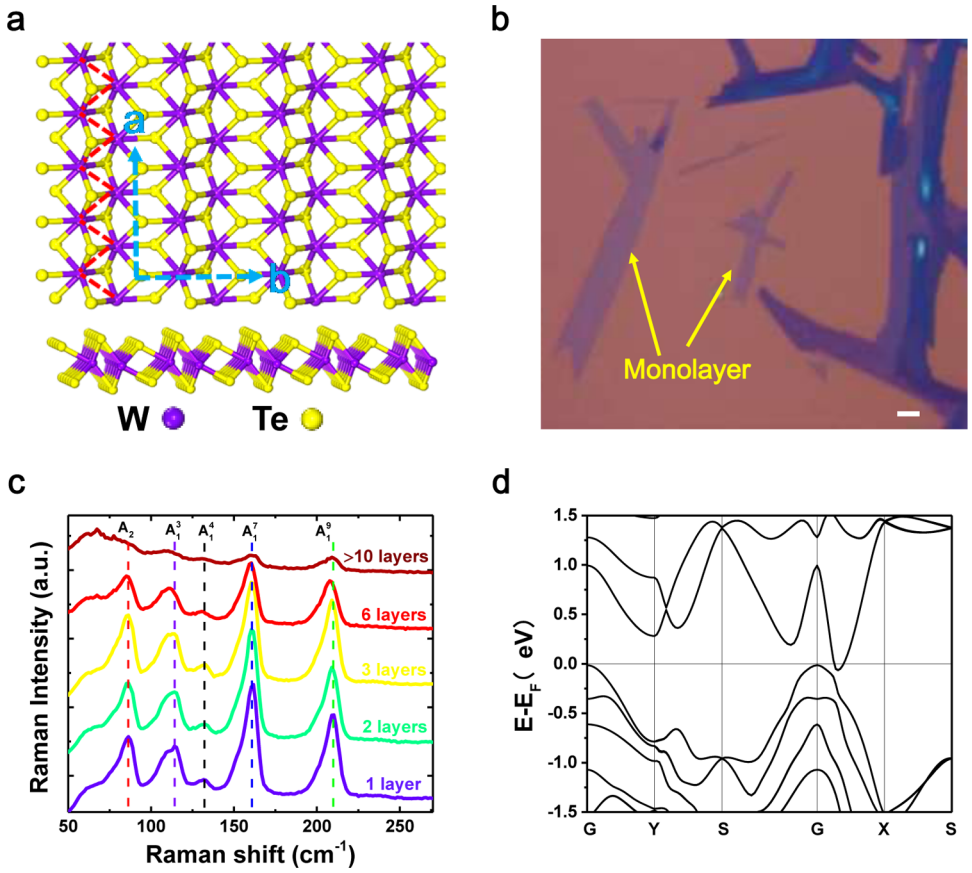

Figure 1. Characterizations of monolayer and few-layer WTe_2 nanosheets grown by CVD. (a) Top: top-view of the crystal structure of WTe_2. Blue dashed line, *a*-axis and *b*-axis of WTe_2 crystal. Bottom: side-view of monolayer WTe_2. (b) Optical image of WTe_2 nanosheets on SiO_2/Si substrate. Scale bar, 8 μm. (c) Raman spectra of the various thickness of WTe_2 on SiO_2/Si substrate. There are shifts of the peak position to the negative direction as the thickness increases. (d) The density functional theory calculated electronic band structure of monolayer WTe_2, indicating no bandgap opening.

shown in Figure 1a, WTe_2 typically crystallizes in an orthorhombic structure (the space group is $Pmn2_1$) in which the tungsten atoms are shifted from their ideal octahedral sites in the octahedron due to the strong intermetallic bonding, forming the zigzag metal−metal chains along the *a*-axis (red dash line).[30] Also, in the distorted octahedral structure the Te atom layers become buckled (lower panel of Figure 1a). Figure 1b provides an optical image of as-grown monolayer and few-layer WTe_2 nanosheets on SiO_2/Si substrate. The largest sample can reach up to 300 × 300 μm^2 (see Supporting Information (SI) Figures S4 and S5). Different thicknesses can be verified through optical contrast and precisely determined by atomic force microscopy. It should be noted that most of the samples were grown with a long-ribbon-like shape (see SI section 2) which is corresponding to the tungsten−tungsten chains in the *a*-axis direction.[7] Figure 1c displays the unpolarized Raman spectra of monolayer and few-layer WTe_2 on SiO_2 substrate. All of the peak positions are consistent with those reported from exfoliated thin flake samples.[24] Also, a small shift to the negative direction of the peak positions is witnessed as the sample thickness increases due to the greater surface effect than the friction effect in WTe_2[31,32] (see SI Figure S3). Moreover, the angular-dependent Raman spectra have been recorded under "parallel" and "perpendicular" polarization configurations, where the Raman peak intensity exhibits a strong periodic angular-dependence, evidencing an anisotropic crystal[10] (see SI section 1 for details). We have also calculated the electronic band structures of double-layer, bulk (SI Figure S6), and monolayer WTe_2. As displayed in Figure 1d, the monolayer WTe_2 shows no bandgap opening, and it maintains a semimetallic state; we will further discuss this point through the transport measurements.

Bulk WTe_2 has been demonstrated to possess nonsaturating MR which may be due to the perfectly compensated electron and hole bands.[3,33] Since the WTe_2 crystal has a layered structure, exotic properties are naturally anticipated as its thickness is reduced to be atomically thin.[34] Back-gated Hall bar devices with various thickness were fabricated by e-beam lithography (EBL), followed by a metal deposition process (see Methods for details). A typical device structure is schematically shown in Figure 2a. The angular-dependent MR was attained by varying the angle between the applied current and the magnetic field as illustrated in Figure 2c inset. The calculated MR ($\mathrm{MR} = \frac{\rho(B)-\rho(0)}{\rho(0)} \times 100\%$) at different θ is shown in Figure 2b and c for the samples with thickness of 2 and 15 nm, respectively. The highest MR values of 120% and 25% for these two samples are significantly lower than those reported from bulk materials[3,4] due to the unequal amount of electron and hole carriers (SI section 6). We also note that the thicker samples do not show a higher MR value compared to the thinner ones which may be due to the dominated quantum correction to the conductance in thin layer WTe_2.[26] The MR of 15 nm sample shows a quadratic relation with B at $|B| > 0.5T$

DOI: 10.1021/acs.nanolett.6b04194
Nano Lett. 2017, 17, 878−885

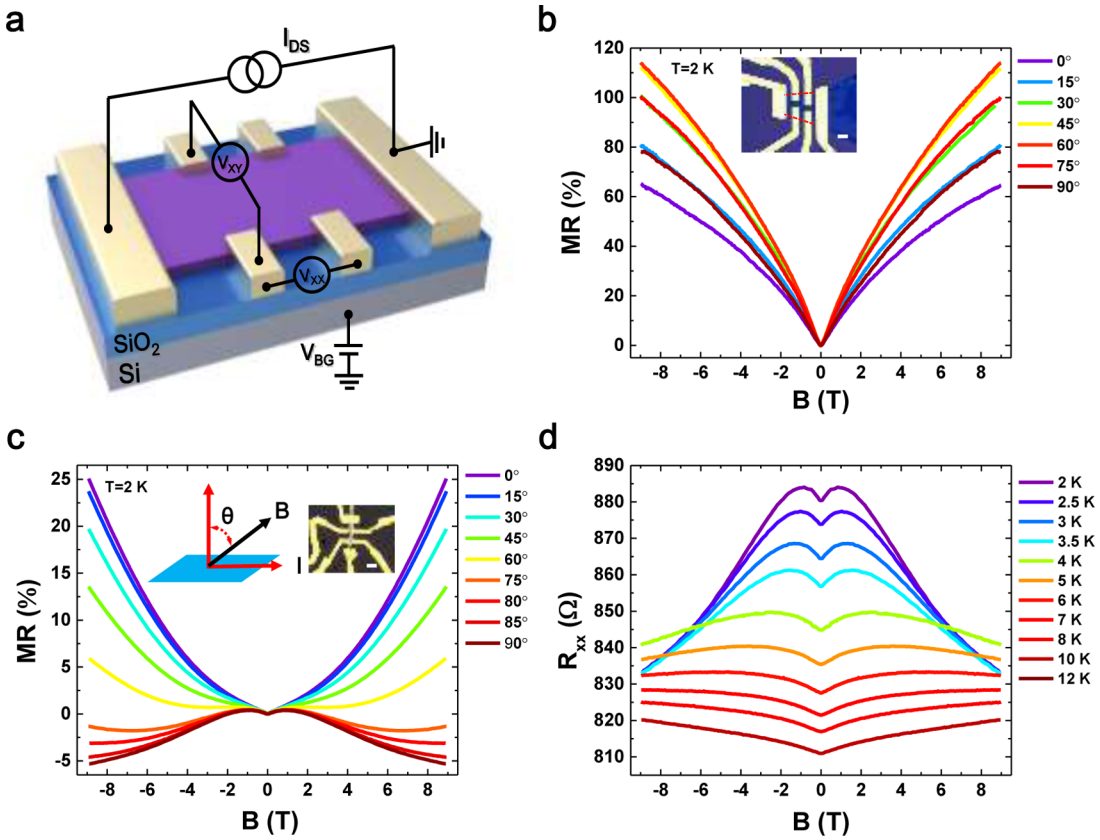

Figure 2. Magneto-transport properties of four-terminal few-layer WTe_2 Hall-bar devices. (a) A schematic structure of WTe_2 back-gated Hall-bar device on SiO_2/Si substrate. (b) Angular-dependent MR of WTe_2 Hall-bar device showing WAL behavior. The channel is 2 nm thick. The inset shows the optical image of the device. Scale bar, 5 μm. (c) Angular-dependent MR of the WTe_2 Hall-bar device showing negative MR when $\theta \geq 75°$. The channel is 15 nm thick. Inset, left, a schematic measurement configuration of titling the angle θ between the sample and applied magnetic field B; right, the optical image of the device. Scale bar, 5 μm. (d) Temperature-dependent MR behavior of the device in panel c at $\theta = 90°$, where the positive MR dominates the entire MR range at $T > 5$ K.

(see SI section 6), while in a small range ($|B| < 0.5T$) the quantum correction to the magnetoconductivity—WAL—emerges.[35,36] The observed WAL behavior is due to the interference of quantum coherent electronic waves undergoing diffusive motion in the presence of spin−orbit interaction, which is large in WTe_2.[26] For the 2 nm sample, the quadratic relation disappears, and the WAL behavior dominates the entire MR range. Interestingly, compared with the 2 nm sample, the 15 nm one shows negative MR (Figure 2c, $|B| > 2T$) when the magnetic field direction is close to that of the applied current (θ approaches 90° in Figure 2c inset). The maximum negative MR is found to be ~6% at $\theta = 90°$ under $B = \pm 9$ T. To verify these experimental results, we have measured over 20 samples with various thickness. In general, with the thickness ~15 nm the negative MR behavior occurs at $\theta = 90°$ with excellent repeatability, while for ~2 nm samples the WAL dominates the entire MR irrespective to the angle θ (Figure 2b, also see SI section 4 for details).

To probe the underlying physics, we have measured the temperature-dependent MR at $\theta = 90°$ (Figure 2d). The negative MR survives up to 5 K (in some devices the negative MR is persistent around 10 K, see SI section 5) above which the positive MR starts to be dominant due to the increase of the thermal-related scatterings.[37] Note that the dips in the small magnetic regime ($|B| < 0.5T$) in Figure 2d are due to the WAL effect originating from the strong spin-obit coupling in WTe_2.[26,38] The negative MR at $|B| > 2T$ can hardly be explained by the WL effect because of the large corresponding magnetic field range.[38−40] As we discuss later, during our experiments we did observe the gate-induced WL behavior in thin samples in a small magnetic regime which is distinct from the nonsaturation negative MR at ±9 T in Figure 2c. We then try to explore other origins of the negative MR in WTe_2. Recently, the negative MR has been observed in Dirac semimetals Cd_3As_2, Na_3Bi, $ZrTe_5$, and Weyl semimetal TaAs due to the chiral anomaly induced charge pumping effect.[37,41−45] In these systems, initially there exists balanced right- and left-handed Fermions having the equal chemical potential ($\mu_R = \mu_L$) for different Weyl nodes. With the electric field parallel to the magnetic field, it induces an imbalance between two chiral nodes, leading to the charge pumping from one Weyl node to the other with opposite chirality.[46] Because of the chiral imbalance ($\mu_R \neq \mu_L$), there is a net current generation in the direction of the electric field that can be described by $j_C = j_{CR} - j_{CL} = \frac{e^2 B}{4\pi^2 \hbar^2}(\mu_R - \mu_L)$;[37,46] thus a negative MR is expected. Since WTe_2 has been theoretically predicted[10] and experimentally evidenced[16−18] to be a type-II Weyl semimetal in which the chiral anomaly exists,[47,48] it is possible that the negative MR observed at $\theta = 90°$ in our study is originated from the chiral anomaly.[42,45,49] Also, the thick WTe_2 sample exhibits as many similar energy bands as the bulk crystal than thin samples;[50] the chiral-anomaly induced negative MR is thus anticipated in relative thick samples,[47,48] which is

DOI: 10.1021/acs.nanolett.6b04194
Nano Lett. 2017, 17, 878−885

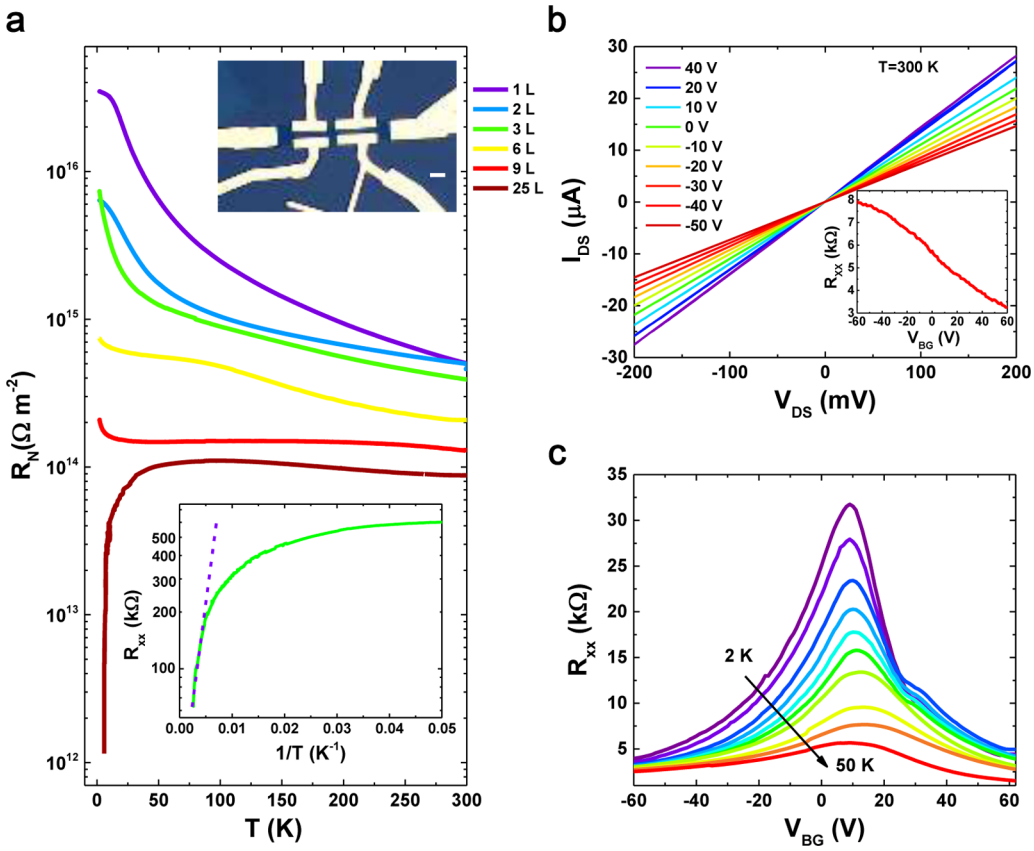

Figure 3. Back-gate field-effect transistors based on few-layer WTe_2. (a) Temperature dependence of the four terminal resistance per square of WTe_2 FET with various channel thicknesses (V_{BG} = 0 V). All of the device shows a semiconducting behavior in the high-temperature regime due to the thermal activation, while for thin samples the weak antilocalization dominates the $R-T$ behavior in the low-temperature regime. Inset, up, an optical image of a few-layer WTe_2 FET device with a channel thickness of 2 nm, scale bar, 3 μm; down, Arrhenius plot of $R_{xx}-T$ of a 2 nm thick device where $E_a \sim 33$ meV can be obtained. (b) Small-range output characteristics ($I_{DS}-V_{DS}$) of a WTe_2 FET device under different V_{BG}, inset, room-temperature transfer curves ($I_{DS}-V_{BG}$) of the device. The channel thickness is 3 nm. (c) Low-temperature transfer curves ($I_{DS}-V_{BG}$) of a 3 nm thick WTe_2 back-gate FET, showing an ambipolar on/off ratio of 10 at both electron and hole sides at 2 K.

also consistent with our experimental results that the negative MR occurs in samples with a thickness around 15 nm. The abundant physics behind the negative MR in WTe_2, however, deserves further investigation.

The transport nature of certain materials changes qualitatively as the thickness decreases from bulk to monolayer. For example, the charge density wave transition temperatures of different thicknesses of $TiSe_2$[51] and TaS_2[52] exhibit dramatic differences. To reveal whether the metallic behavior in WTe_2 bulk material will still hold when its thickness goes down to monolayer or few layers, we measured the temperature-dependent resistance ($R-T$) of CVD-grown WTe_2. Figure 3a shows the normalized square resistance of the samples with various thicknesses. Interestingly, thicker samples show metal-to-insulator transition—in the high temperature regime, the resistance increases as the temperature decreases, while in the low temperature regime the opposite trend is observed. For the thinner samples, the insulating behavior dominates the entire $R-T$ curve. We believe that the semiconducting-like behavior in the high temperature regime for our CVD-grown WTe_2 is originated from the low carrier density[37] (see SI section 7) and can be interpreted by the thermal activation mechanism.[53] Due to the gapless energy band of WTe_2 (as shown in Figure 1d and SI Figure S6), the holes in the valence band can be thermally activated when the Fermi level is close to the Dirac point. The thermal activation is reduced as the temperature decreases, leading to the semiconducting-like $R-T$ behavior in the high temperature regime.[37] After reaching a critical temperature, the thermal energy is not sufficient to excite electrons to the conduction band above the Fermi level, resulting in a metallic-like $R-T$ at low temperatures. Meanwhile, for the thinner samples, the semiconducting-like behavior at low temperatures comes from the Anderson localization.[54] We have fitted the high temperature resistance of a 2 nm thick WTe_2 device to the thermal activation equation $R_{xx} \sim \exp(E_a/k_BT)$; the calculated thermal activation energy E_a is about 33 meV (Figure 3a inset).

Next, we investigate the temperature-dependent transport properties of atomically thin WTe_2 using back-gated four-terminal devices (Inset of Figure 2a). For this type of device, the measured four-probe resistance is defined as $R = (V_1 - V_2)/I_{DS}$, where I_{DS} is the source−drain current and $V_1 - V_2$ is the measured voltage drop between the middle two voltage probes. Figure 3b shows a typical four-terminal $I_{DS}-V_{DS}$ of the 3 nm thick WTe_2 field-effect transistor (FET) device under various back-gate voltages (V_{BG}) at room temperature. The symmetric linear $I_{DS}-V_{DS}$ curves indicate that a well-defined Ohmic contact has been developed between the electrodes and WTe_2.[55] The transfer curves at room temperature ($I_{DS}-V_{BG}$) are shown in the inset of Figure 3b. As the back gate sweeps from −60 to 60 V, the resistance changes ~2.5 times, indicating an n-type conduction. Then we studied the transfer curves of WTe_2 FET devices at lower temperatures. Interestingly, the

DOI: 10.1021/acs.nanolett.6b04194
Nano Lett. 2017, 17, 878−885

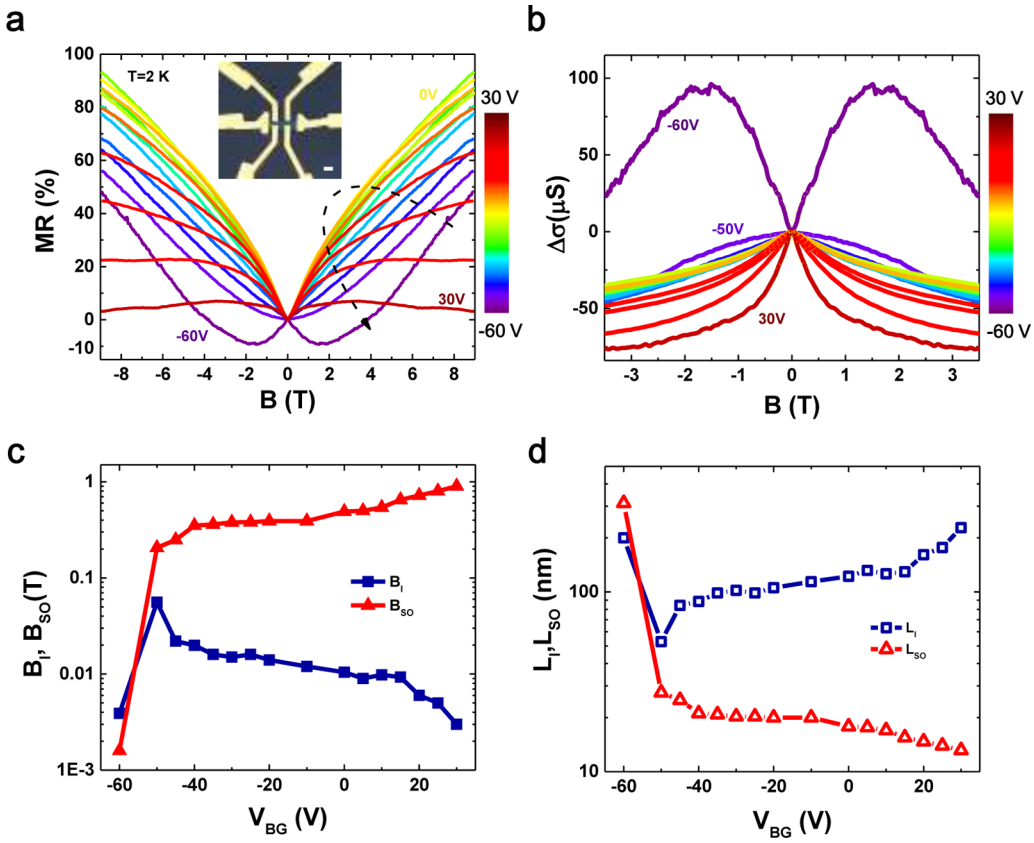

Figure 4. Gate-tunable WAL−WL crossover in few-layer WTe_2 device. (a) Low-temperature gate-dependent MR behavior of WTe_2 device with channel thickness of 7 nm, where both the positive and negative V_{BG} can effectively tune the MR. A WL (negative MR) behavior happens at V_{BG} = −60 V. Inset, optical image of the device, scale bar, 5 μm. (b) Magnetoconductivity of the device under different V_{BG}, where a WAL−WL transition can be clearly seen. The yellow dots show the fitting of the data to the MF localization equation. (c) The deduced B_I and B_{SO} of the device under different V_{BG}. (d) Calculated L_I and L_{SO} of the device under different V_{BG}.

transfer curves show a strong well-defined ambipolar behavior at the reduced temperatures. The on/off ratio (the ratio between the maximum and minimum resistance value) can reach up to 10 at 2 K both at electron and hole sides and drops as the temperature increases, implying that the electronic states in the WTe_2 channel can be effectively modulated by V_{BG}. It should be noted that the asymmetric behavior of the hole and electron accumulation in Figure 3c may come from the asymmetric electron and hole states of the conduction and valence band[53] (also see SI section 6 for details). Our study demonstrates the first ambipolar WTe_2-based FET device. It is believed that further improvement of the FET performance can be done by using high-κ dielectric oxides like Al_2O_3 or HfO_2.[56]

The strong spin−orbit interaction (SOI) and ambipolar gate modulation in WTe_2 inspire us to perform the gate-dependent magnetotransport measurements to probe the electric-field modulation of the MR and SOI.[57] Figure 4a depicts the MR behavior of a 7 nm thick sample with V_{BG} changing from −60 to 30 V. Interestingly, the MR ratio is reduced both at positive and negative V_{BG} compared to zero gate voltage (yellow curve in Figure 4a). Surprisingly, a negative MR − weak localization− occurs when V_{BG} = −60 V at $|B| < 2$T. We believe that the negative MR at V_{BG} = −60 V is most likely due to the gate modulation of the SOI since the MR value can never be negative according to the two band theory (see SI section 6 for details). In Figure 4b, we plot the $\Delta\sigma = \sigma(B) - \sigma(0)$ under various V_{BG}, where a clear WAL to WL transition occurs as V_{BG} sweeps from 30 to −60 V. Here σ and B are the sheet conductance and the perpendicular magnetic field ($\theta = 0°$ in Figure 2c inset). To understand the crossover from WAL to WL quantitatively, we analyzed the observed magnetoresistance using the Maekawa and Fukuyama (MF) localization equation:[58]

$$\Delta\sigma(B) = \frac{e^2}{\pi h}\left[\psi\left(\frac{B}{B_I + B_{SO}}\right) + \frac{1}{2\sqrt{1-\gamma^2}}\psi\left(\frac{B}{B_I + B_{SO}(1+\sqrt{1-\gamma^2})}\right) - \frac{1}{2\sqrt{1-\gamma^2}}\psi\left(\frac{B}{B_I + B_{SO}(1-\sqrt{1-\gamma^2})}\right)\right] \quad (1)$$

Here, the function ψ is defined as $\psi(x) = \ln(x) + \psi\left(\frac{1}{2} + \frac{1}{x}\right)$, where $\psi(x)$ is the digamma function. The parameters[59] of the equation contain inelastic field $B_I = \hbar/(4el_I^2)$, spin−orbit field $B_{SO} = \hbar/(4el_{SO}^2)$ and Zeeman correction term γ, where l_I and l_{SO} are the Thouless inelastic length and spin−orbit diffusion length, respectively. As shown in Figure 4b (yellow short dots), the fitting result agrees well with the experimental data. According to Figure 4c, B_I has a maximum value at V_{BG} = −50 V and decreases as V_{BG} increases from −50 to 30 V, while B_{SO} increases monotonically as V_{BG} increases, in a good agreement with our scenario of the gate tunability of SOI. The

DOI: 10.1021/acs.nanolett.6b04194
Nano Lett. 2017, 17, 878−885

corresponding l_I and l_{SO} are shown in Figure 4d; l_I reaches a minimum value at $V_{BG} = -50$ V and increases from 52 to 228 nm as V_{BG} changes from −50 to 30 V, while l_{SO} decreases monotonically from 310 to 13 nm as V_{BG} increases, indicating a good gate tunability. At large negative V_{BG} ($V_{BG} = -60$ V), l_I is smaller than l_{SO}, suggesting that the effect of spin−orbit coupling is weak compared with the orbital effect of the magnetic field. As a result, the WAL−WL crossover takes place. Also, we have used Hikami−Larkin−Nagaoka (HLN) equation[60] to fit the gate tunable MR, where the fitting parameter α changes from positive to negative value at $V_{BG} = -60$ V, giving rise to the WAL−WL transition (see SI section 9 for details). It should be noted that the magnetic field here is perpendicular to the applied current during the measurement ($\theta = 0°$ in Figure 2c inset); thus, the gate induced negative MR could not come from the chiral anomaly (the angle-dependent MR at $V_{BG} = -60$ V is shown in Figure S11c, where the negative MR happens only in the magnetic field range $|B| < 2$ T, showing different behavior compared to the chiral anomaly induced negative MR in Figure 2c). We also note that such a WAL−WL transition shows similar phenomena in oxide interfaces with Rashba spin-obit interaction,[61] which cannot be explained by the classical two band theory (see SI material section 6).[33,62] At this stage, the exquisite physics in WTe_2 nanostructures deserves further theoretical investigations.

In summary, we have successfully synthesized mono- and few-layer WTe_2 via a CVD method. The high-quality as-grown thick samples allow us to observe the negative MR when the applied magnetic field is parallel to the electric field. Also, we have incorporated few-layer WTe_2 into FET devices which show prominent ambipolar behavior. More importantly, the SOI in WTe_2 could be effectively tuned by the applied electric field, resulting in a WAL−WL transition in magnetoresistivity. Our results shed the light on the applications of WTe_2 in practical and versatile electronic devices.

Methods. *Sample Synthesis.* Monolayer and few-layer WTe_2 crystals were synthesized in a horizontal tube furnace equipped with a 1-in.-diameter quartz tube. One-nm-thick tungsten was deposited onto SiO_2 (100 nm)/Si substrates using magnetic sputtering to act as precursor for the subsequent CVD growth. After that, W(1 nm)/SiO_2(100 nm)/Si substrates were loaded into the center region of the furnace (see Figure S3a). A crucible containing 50 mg of tellurium powder (≥99.9% Alfa Aesar) was located upstream. Argon(90%)/H_2(10%)/mixed gases were kept at a flow rate of 70 sccm at ambient pressure serving as the carrying gas. During the growth, the tube furnace was heated to 760 °C within 40 min. After maintaining at 760 °C for 10 min, the system was naturally cooled down to room temperature.

Polarization-Dependent Raman Spectroscopy. A polarizer was placed between an edge filter and a spectrometer to keep the angle between the incident light polarizer and the polarizer set in front of the spectrometer 0°, thus obtaining the parallel polarization configuration. The cross-polarization condition was achieved by rotating the two polarizers to set the angle 90°.

Back-Gate Hall-Bar and FET Devices for Transport Measurements. After the CVD growth process, the synthesized WTe_2 was spin-coated with PMMA/MMA bilayer polymer immediately to protect the sample from oxidation. An EBL process was performed first to make the markers for the subsequent EBL alignment (see Figure S4); then the electrical contacts of WTe_2 back-gate devices were fabricated using another EBL process. Ti/Au (5 nm/100 nm) electrodes were then deposited using magnetic sputtering. Four-terminal temperature-dependent magnetotransport measurements were carried out in a Physical Property Measurement System (PPMS) system (Quantum Design) using lock-in amplifier (SR830) and Agilent 2912.

First-Principles Calculations. Band structure of bulk and monolayer WTe_2 were calculated in the framework of density functional theory (DFT) using the Vienna ab initio simulation package (VASP)[63] with projector augmented wave (PAW). Exchange-correlation potential is treated within the generalized gradient approximation (GGA) of Perdew−Becke−Ernzerhof (PBE) type.[64] Spin−orbit coupling (SOC) is taken into account in self-consistency. The cutoff energy for plane wave expansion is 300 eV, and irreducible Brillouin zone was sampled by a 12 × 10 × 6 (bulk) and 10 × 5 × 1 (monolayer) mesh of k-points. The monolayer was gapped by a 15 Å vacuum in the c direction.

■ ASSOCIATED CONTENT

Supporting Information

The Supporting Information is available free of charge on the ACS Publications website at DOI: 10.1021/acs.nanolett.6b04194.

Polarization- and thickness-dependent Raman spectra of WTe_2, details of CVD-grown WTe_2 and device fabrication process, band structures of double-layer and bulk WTe_2, evolution of quantum localization in various thickness WTe_2, another WTe_2 device with negative MR, gate-tunable Hall signals and its relation with ambipolar properties, typical temperature-dependent carrier density and Hall mobility in thin layer WTe_2 additional information for the device in the main text showing gate-tunable WAL-WL transition, and HLN fitting of the gate-tunable WAL−WL transition (PDF)

■ AUTHOR INFORMATION

Corresponding Author

*E-mail: Faxian@fudan.edu.cn.

ORCID

Faxian Xiu: 0000-0003-2860-0369

Notes

The authors declare no competing financial interest.

■ ACKNOWLEDGMENTS

This work was supported by the National Young 1000 Talent Plan and National Natural Science Foundation of China (61322407, 11474058, and 61674040). Part of the sample fabrication was performed at Fudan Nanofabrication Laboratory.

■ REFERENCES

(1) Geim, A. K.; Novoselov, K. S. *Nat. Mater.* **2007**, *6* (3), 183−191.

(2) Wang, Q. H.; Kalantar-Zadeh, K.; Kis, A.; Coleman, J. N.; Strano, M. S. *Nat. Nanotechnol.* **2012**, *7* (11), 699−712.

(3) Ali, M. N.; Xiong, J.; Flynn, S.; Tao, J.; Gibson, Q. D.; Schoop, L. M.; Liang, T.; Haldolaarachchige, N.; Hirschberger, M.; Ong, N. P.; Cava, R. J. *Nature* **2014**, *514* (7521), 205−8.

(4) Cai, P. L.; Hu, J.; He, L. P.; Pan, J.; Hong, X. C.; Zhang, Z.; Zhang, J.; Wei, J.; Mao, Z. Q.; Li, S. Y. *Phys. Rev. Lett.* **2015**, *115* (5), 057202.

(5) Zhu, Z.; Lin, X.; Liu, J.; Fauque, B.; Tao, Q.; Yang, C.; Shi, Y.; Behnia, K. *Phys. Rev. Lett.* **2015**, *114* (17), 176601.

DOI: 10.1021/acs.nanolett.6b04194
Nano Lett. 2017, 17, 878−885

(6) Rhodes, D.; Das, S.; Zhang, Q. R.; Zeng, B.; Pradhan, N. R.; Kikugawa, N.; Manousakis, E.; Balicas, L. *Phys. Rev. B: Condens. Matter Mater. Phys.* **2015**, *92* (12), 125152.
(7) Zhao, Y.; Liu, H.; Yan, J.; An, W.; Liu, J.; Zhang, X.; Wang, H.; Liu, Y.; Jiang, H.; Li, Q. *Phys. Rev. B: Condens. Matter Mater. Phys.* **2015**, *92* (4), 041104.
(8) Jiang, J.; Tang, F.; Pan, X.; Liu, H.; Niu, X.; Wang, Y.; Xu, D.; Yang, H.; Xie, B.; Song, F. *Phys. Rev. Lett.* **2015**, *115* (16), 166601.
(9) Pletikosić, I.; Ali, M. N.; Fedorov, A.; Cava, R.; Valla, T. *Phys. Rev. Lett.* **2014**, *113* (21), 216601.
(10) Soluyanov, A. A.; Gresch, D.; Wang, Z.; Wu, Q.; Troyer, M.; Dai, X.; Bernevig, B. A. *Nature* **2015**, *527* (7579), 495−8.
(11) Chang, T. R.; Xu, S. Y.; Chang, G.; Lee, C. C.; Huang, S. M.; Wang, B.; Bian, G.; Zheng, H.; Sanchez, D. S.; Belopolski, I.; Alidoust, N.; Neupane, M.; Bansil, A.; Jeng, H. T.; Lin, H.; Zahid Hasan, M. *Nat. Commun.* **2016**, *7*, 10639.
(12) Belopolski, I.; Xu, S.-Y.; Ishida, Y.; Pan, X.; Yu, P.; Sanchez, D. S.; Neupane, M.; Alidoust, N.; Chang, G.; Chang, T.-R.; Wu, Y.; Bian, G.; Zheng, H.; Huang, S.-M.; Lee, C.-C.; Mou, D.; Huang, L.; Song, Y.; Wang, B.; Wang, G.; Yeh, Y.-W.; Yao, N.; Rault, J. E.; Le Fèvre, P.; Bertran, F.; Jeng, H.-T.; Kondo, T.; Kaminski, A.; Lin, H.; Liu, Z.; Song, F.; Shin, S.; Hasan, M. Z. arXiv preprint. *arXiv*:1512.09099, **2015**.
(13) Deng, K.; Wan, G.; Deng, P.; Zhang, K.; Ding, S.; Wang, E.; Yan, M.; Huang, H.; Zhang, H.; Xu, Z.; Denlinger, J.; Fedorov, A.; Yang, H.; Duan, W.; Yao, H.; Wu, Y.; Fan, S.; Zhang, H.; Chen, X.; Zhou, S. *Nat. Phys.* **2016**, *12* (12), 1105−1110.
(14) Jiang, J.; Liu, Z.; Sun, Y.; Yang, H.; Rajamathi, R.; Qi, Y.; Yang, L.; Chen, C.; Peng, H.; Hwang, C.-C.; Sun, S. Z.; Mo, S.-K.; Vobornik, I.; Fujii, J.; Parkin, S. S. P.; Felser, C.; Yan, B. H.; Chen, Y. L. arXiv preprint. *arXiv*: 1604.00139, **2016**.
(15) Liang, A.; Huang, J.; Nie, S.; Ding, Y.; Gao, Q.; Hu, C.; He, S.; Zhang, Y.; Wang, C.; Shen, B.; Liu, J.; Ai, P.; Yu, L.; Sun, X.; Zhao, W.; Lv, S.; Liu, D.; Li, C.; Zhang, Y.; Hu, Y.; Xu, Y.; Zhao, L.; Liu, G.; Mao, Z.; Jia, X.; Zhang, F.; Zhang, S.; Yang, F.; Wang, Z.; Peng, Q.; Weng, H.; Dai, X.; Fang, Z.; Xu, Z.; Chen, C.; Zhou, X. J. arXiv preprint. *arXiv*: 1604.01706, **2016**.
(16) Bruno, F. Y.; Tamai, A.; Wu, Q. S.; Cucchi, I.; Barreteau, C.; de la Torre, A.; McKeown Walker, S.; Riccò, S.; Wang, Z.; Kim, T. K.; Hoesch, M.; Shi, M.; Plumb, N. C.; Giannini, E.; Soluyanov, A. A.; Baumberger, F. *Phys. Rev. B: Condens. Matter Mater. Phys.* **2016**, *94* (12), 121112.
(17) Wang, C.; Zhang, Y.; Huang, J.; Nie, S.; Liu, G.; Liang, A.; Zhang, Y.; Shen, B.; Liu, J.; Hu, C.; Ding, Y.; Liu, D.; Hu, Y.; He, S.; Zhao, L.; Yu, L.; Hu, J.; Wei, J.; Mao, Z.; Shi, Y.; Jia, X.; Zhang, F.; Zhang, S.; Yang, F.; Wang, Z.; Peng, Q.; Weng, H.; Dai, X.; Fang, Z.; Xu, Z.; Chen, C.; Zhou, X. J. arXiv preprint. *arXiv*: 1604.04218, **2016**.
(18) Wu, Y.; Mou, D.; Jo, N. H.; Sun, K.; Huang, L.; Bud'ko, S. L.; Canfield, P. C.; Kaminski, A. *Phys. Rev. B: Condens. Matter Mater. Phys.* **2016**, *94* (12), 121113.
(19) Belopolski, I.; Xu, S.-Y.; Ishida, Y.; Pan, X.; Yu, P.; Sanchez, D. S.; Zheng, H.; Neupane, M.; Alidoust, N.; Chang, G.; Chang, T.-R.; Wu, Y.; Bian, G.; Huang, S.-M.; Lee, C.-C.; Mou, D.; Huang, L.; Song, Y.; Wang, B.; Wang, G.; Yeh, Y.-W.; Yao, N.; Rault, J. E.; Le Fèvre, P.; Bertran, F.; Jeng, H.-T.; Kondo, T.; Kaminski, A.; Lin, H.; Liu, Z.; Song, F.; Shin, S.; Hasan, M. Z. *Phys. Rev. B: Condens. Matter Mater. Phys.* **2016**, *94* (8), 085127.
(20) Tamai, A.; Wu, Q. S.; Cucchi, I.; Bruno, F. Y.; Riccò, S.; Kim, T. K.; Hoesch, M.; Barreteau, C.; Giannini, E.; Besnard, C.; Soluyanov, A. A.; Baumberger, F. *Phys. Rev. X* **2016**, *6* (3), 031021.
(21) Huang, L.; McCormick, T. M.; Ochi, M.; Zhao, Z.; Suzuki, M. T.; Arita, R.; Wu, Y.; Mou, D.; Cao, H.; Yan, J.; Trivedi, N.; Kaminski, A. *Nat. Mater.* **2016**, *15*, 1155.
(22) Qian, X.; Liu, J.; Fu, L.; Li, J. *Science* **2014**, *346* (6215), 1344−1347.
(23) Zheng, F.; Cai, C.; Ge, S.; Zhang, X.; Liu, X.; Lu, H.; Zhang, Y.; Qiu, J.; Taniguchi, T.; Watanabe, K.; Jia, S.; Qi, J.; Chen, J. H.; Sun, D.; Feng, J. *Adv. Mater.* **2016**, *28* (24), 4845−4851.
(24) Kong, W. D.; Wu, S. F.; Richard, P.; Lian, C. S.; Wang, J. T.; Yang, C. L.; Shi, Y. G.; Ding, H. *Appl. Phys. Lett.* **2015**, *106* (8), 081906.
(25) Jiang, Y. C.; Gao, J.; Wang, L. *Sci. Rep.* **2016**, *6*, 19624.
(26) Wang, L.; Gutierrez-Lezama, I.; Barreteau, C.; Ubrig, N.; Giannini, E.; Morpurgo, A. F. *Nat. Commun.* **2015**, *6*, 8892.
(27) Wang, Y.; Wang, K.; Reutt-Robey, J.; Paglione, J.; Fuhrer, M. S. *Phys. Rev. B: Condens. Matter Mater. Phys.* **2016**, *93* (12), 121108.
(28) Lin, Y.-M.; Valdes-Garcia, A.; Han, S.-J.; Farmer, D. B.; Meric, I.; Sun, Y.; Wu, Y.; Dimitrakopoulos, C.; Grill, A.; Avouris, P. *Science* **2011**, *332* (6035), 1294−1297.
(29) Kang, K.; Xie, S.; Huang, L.; Han, Y.; Huang, P. Y.; Mak, K. F.; Kim, C.-J.; Muller, D.; Park, J. *Nature* **2015**, *520* (7549), 656−660.
(30) Brown, B. E. *Acta Crystallogr.* **1966**, *20* (2), 268−274.
(31) Kim, Y.; Jhon, Y. I.; Park, J.; Kim, J. H.; Lee, S.; Jhon, Y. M. *Nanoscale* **2016**, *8* (4), 2309−2316.
(32) Liang, L.; Meunier, V. *Nanoscale* **2014**, *6* (10), 5394−5401.
(33) Lv, H.; Lu, W.; Shao, D.; Liu, Y.; Tan, S.; Sun, Y. *Europhys. Lett.* **2015**, *110* (3), 37004.
(34) Das, P. K.; Di Sante, D.; Vobornik, I.; Fujii, J.; Okuda, T.; Bruyer, E.; Gyenis, A.; Feldman, B. E.; Tao, J.; Ciancio, R.; Rossi, G.; Ali, M. N.; Picozzi, S.; Yadzani, A.; Panaccione, G.; Cava, R. J. *Nat. Commun.* **2016**, *7*, 10847.
(35) Naylor, C. H.; Parkin, W. M.; Ping, J.; Gao, Z.; Zhou, Y. R.; Kim, Y.; Streller, F.; Carpick, R. W.; Rappe, A. M.; Drndic, M.; Kikkawa, J. M.; Johnson, A. T. *Nano Lett.* **2016**, *16* (7), 4297−304.
(36) Zhou, J.; Liu, F.; Lin, J.; Huang, X.; Xia, J.; Zhang, B.; Zeng, Q.; Wang, H.; Zhu, C.; Niu, L.; Wang, X.; Fu, W.; Yu, P.; Chang, T. R.; Hsu, C. H.; Wu, D.; Jeng, H. T.; Huang, Y.; Lin, H.; Shen, Z.; Yang, C.; Lu, L.; Suenaga, K.; Zhou, W.; Pantelides, S. T.; Liu, G.; Liu, Z. arXiv preprint. *arXiv*: 1606.00126, **2016**.
(37) Li, C. Z.; Wang, L. X.; Liu, H.; Wang, J.; Liao, Z. M.; Yu, D. P. *Nat. Commun.* **2015**, *6*, 10137.
(38) Kim, H. J.; Kim, K. S.; Wang, J. F.; Sasaki, M.; Satoh, N.; Ohnishi, A.; Kitaura, M.; Yang, M.; Li, L. *Phys. Rev. Lett.* **2013**, *111* (24), 246603.
(39) Zhang, C.; Zhang, E.; Liu, Y.; Chen, Z.-G.; Liang, S.; Cao, J.; Yuan, X.; Tang, L.; Li, Q.; Gu, T.; Wu, Y.; Zou, J.; Xiu, F. arXiv preprint. *arXiv*: 1504.07698, **2015**.
(40) Xu, X.-T.; Jia, S. *Chin. Phys. B* **2016**, *25* (11), 117204−117204.
(41) Du, J. H.; Wang, H. D.; Chen, Q.; Mao, Q. H.; Khan, R.; Xu, B. J.; Zhou, Y. X.; Zhang, Y. N.; Yang, J. H.; Chen, B.; Feng, C.; Fang, M. *Sci. China: Phys., Mech. Astron.* **2016**, *59* (15), 1−6.
(42) Li, Y.; Li, L.; Wang, J.; Wang, T.; Xu, X.; Xi, C.; Cao, C.; Dai, J. *Phys. Rev. B: Condens. Matter Mater. Phys.* **2016**, *94* (12), 121115.
(43) Li, H.; He, H.; Lu, H. Z.; Zhang, H.; Liu, H.; Ma, R.; Fan, Z.; Shen, S. Q.; Wang, J. *Nat. Commun.* **2016**, *7*, 10301.
(44) Li, Q.; Kharzeev, D. E.; Zhang, C.; Huang, Y.; Pletikosić, I.; Fedorov, A. V.; Zhong, R. D.; Schneeloch, J. A.; Gu, G. D.; Valla, T. *Nat. Phys.* **2016**, *12* (6), 550−554.
(45) Huang, X.; Zhao, L.; Long, Y.; Wang, P.; Chen, D.; Yang, Z.; Liang, H.; Xue, M.; Weng, H.; Fang, Z.; Dai, X.; Chen, G. *Phys. Rev. X* **2015**, *5* (3), 031023.
(46) Parameswaran, S.; Grover, T.; Abanin, D.; Pesin, D.; Vishwanath, A. *Phys. Rev. X* **2014**, *4* (3), 031035.
(47) Wang, Y.; Liu, E.; Liu, H.; Pan, Y.; Zhang, L.; Zeng, J.; Fu, Y.; Wang, M.; Xu, K.; Huang, Z.; Wang, Z.; Lu, H. Z.; Xing, D.; Wang, B.; Wan, X.; Miao, F. *Nat. Commun.* **2016**, *7* (8), 13142.
(48) Sharma, G.; Goswami, P.; Tewari, S. arXiv preprint. *arXiv*: 1608.06625, **2016**.
(49) Zhang, C. L.; Xu, S. Y.; Belopolski, I.; Yuan, Z.; Lin, Z.; Tong, B.; Bian, G.; Alidoust, N.; Lee, C. C.; Huang, S. M.; Chang, T. R.; Chang, G.; Hsu, C. H.; Jeng, H. T.; Neupane, M.; Sanchez, D. S.; Zheng, H.; Wang, J.; Lin, H.; Zhang, C.; Lu, H. Z.; Shen, S. Q.; Neupert, T.; Zahid Hasan, M.; Jia, S. *Nat. Commun.* **2016**, *7*, 10735.
(50) Wang, L.; Gutiérrez-Lezama, I.; Barreteau, C.; Ki, D.-K.; Giannini, E.; Morpurgo, A. F. *Phys. Rev. Lett.* **2016**, *117* (17), 176601.
(51) Li, L. J.; O'Farrell, E. C.; Loh, K. P.; Eda, G.; Ozyilmaz, B.; Castro Neto, A. H. *Nature* **2015**, *529* (7585), 185−9.

DOI: 10.1021/acs.nanolett.6b04194
Nano Lett. 2017, 17, 878−885

(52) Yu, Y.; Yang, F.; Lu, X. F.; Yan, Y. J.; Cho, Y. H.; Ma, L.; Niu, X.; Kim, S.; Son, Y. W.; Feng, D.; Li, S.; Cheong, S. W.; Chen, X. H.; Zhang, Y. *Nat. Nanotechnol.* **2015**, *10* (3), 270−6.
(53) Li, C.-Z.; Li, J.-G.; Wang, L.-X.; Zhang, L.; Zhang, J.-M.; Yu, D.; Liao, Z.-M. *ACS Nano* **2016**, *10* (6), 6020−6028.
(54) Bergmann, G. *Phys. Rep.* **1984**, *107* (1), 1−58.
(55) Radisavljevic, B.; Radenovic, A.; Brivio, J.; Giacometti, V.; Kis, A. *Nat. Nanotechnol.* **2011**, *6* (3), 147−50.
(56) Radisavljevic, B.; Kis, A. *Nat. Mater.* **2013**, *12* (9), 815−820.
(57) Yuan, H.; Bahramy, M. S.; Morimoto, K.; Wu, S.; Nomura, K.; Yang, B.-J.; Shimotani, H.; Suzuki, R.; Toh, M.; Kloc, C.; Xu, X.; Arita, R.; Nagaosa, N.; Iwasa, Y. *Nat. Phys.* **2013**, *9* (9), 563−569.
(58) Maekawa, S.; Fukuyama, H. *J. Phys. Soc. Jpn.* **1981**, *50* (8), 2516−2524.
(59) Lee, P. A.; Ramakrishnan, T. V. *Rev. Mod. Phys.* **1985**, *57* (2), 287−337.
(60) Chen, J.; Qin, H. J.; Yang, F.; Liu, J.; Guan, T.; Qu, F. M.; Zhang, G. H.; Shi, J. R.; Xie, X. C.; Yang, C. L.; Wu, K. H.; Li, Y. Q.; Lu, L. *Phys. Rev. Lett.* **2010**, *105* (17), 176602.
(61) Caviglia, A.; Gabay, M.; Gariglio, S.; Reyren, N.; Cancellieri, C.; Triscone, J.-M. *Phys. Rev. Lett.* **2010**, *104* (12), 126803.
(62) Hurd, C. M. *The Hall effect in metals and alloys*; Plenum Press: New York, 1976.
(63) Kresse, G.; Furthmüller, J. *Phys. Rev. B: Condens. Matter Mater. Phys.* **1996**, *54* (16), 11169.
(64) Perdew, J. P.; Burke, K.; Ernzerhof, M. *Phys. Rev. Lett.* **1996**, *77* (18), 3865.

■ NOTE ADDED AFTER ASAP PUBLICATION

This paper was published on the Web on January 3, 2017. Reference 47 was replaced, and the corrected version was reposted on January 5, 2017.

DOI: 10.1021/acs.nanolett.6b04194
Nano Lett. 2017, 17, 878−885